Supporting Information for

Overriding plate thickness as a controlling factor for trench retreat rates in narrow subduction zones

Pedro J. Gea[1,2], Flor de Lis Mancilla[1,2], Ana M. Negredo[3,4], and Jeroen van Hunen[5]

[1]Department of Theoretical Physics and Cosmology, University of Granada, Granada, Spain
[2]Andalusian Institute of Geophysics, University of Granada, Granada, Spain
[3]Department of Earth Physics and Astrophysics, Complutense University of Madrid, Madrid, Spain
[4]Institute of Geosciences IGEO (CSIC, UCM), Madrid, Spain
[5]Department of Earth Sciences, Durham University, DH1 3LE Durham, UK

Contents of this file

1. Text S1 to S2
2. Figures S1 to S2
3. Tables S1 to S3

Introduction

Text S1 describes the basic equations and Text S2 summarizes the rheological model. Figure S1 shows an example of model evolution for a slab width of 600 km. Figure S2 ilustrates the effect of the viscous coupling at the lateral slab edge on trench geometry. Table S1 contains the model parameters used in the numerical simulations. Tabla S2 summarizes the parameters tested in the numerical experiments. Table S3 includes the data used in Figure 4 with their references.

Text S1. Numerical method

We use version 2.4.0 of the finite-element code ASPECT (Advanced Solver for Problems in Earth's ConvecTion) (Kronbichler et al., 2012; Heister et al., 2017; Gassmöller et al., 2018; Bangerth et al., 2021a, 2021b) to simulate 3D self-consistent subduction models. The momentum, mass, and energy conservation equations for an incompressible fluid are solved using the Boussinesq approximation:

$$\nabla \cdot \mathbf{u} = 0 \tag{1}$$

$$-\nabla \cdot 2\mu\dot{\varepsilon}\left(\mathbf{u}\right) + \nabla P = \rho\mathbf{g} \tag{2}$$

$$\rho_o c_p \left(\frac{\partial T}{\partial t} + \mathbf{u} \cdot \nabla T\right) - \nabla \cdot k\nabla T = \rho_o H \tag{3}$$

where $\dot{\varepsilon} = \frac{1}{2}\left(\nabla\mathbf{u} + \nabla\mathbf{u}^T\right)$ is the strain rate tensor, ρ is the density, μ is the viscosity, P is the pressure, $\mathbf{u}$ is the velocity, $\mathbf{g}$ is the gravitational acceleration, c_p is the specific heat, T is the temperature, k is the thermal conductivity, ρ_o is the density at a reference temperature T_o and H is the radiogenic heating, which is neglected in our models.

Besides these equations, ASPECT solves the advection of compositional fields c_i, which are used to track materials and their properties throughout the simulations:

$$\frac{\partial c_i}{\partial t} + \mathbf{u} \cdot \nabla c_i = 0 \tag{4}$$

Text S2. Rheological model

We use a temperature-dependent rheology in which the viscosity is given by:

$$\mu = \frac{1}{2A} d^m \exp\left(\frac{E + PV}{RT}\right) \tag{5}$$

where A is a prefactor of the equation, d is the grain size, m is the grain size exponent, E is the activation energy, V is the activation volume, P is the pressure and R is the gas constant.

For the upper mantle (asthenosphere and lithosphere) we use rheological parameters from wet olivine (Hirth & Kohlstedt, 2003). With these parameters, we obtain a viscosity of $1.57 \cdot 10^{20}$ Pa s at a depth of 150 km. For the overriding plate crust we adopt rheological parameters from wet anorthite feldspar (Bürgmann & Dresen, 2008). The temperature-dependent viscosity is capped by a preset minimum and a maximum viscosity of 10^{19} and $1.57 \cdot 10^{23}$ Pa s respectively to avoid large viscosity jumps. For the oceanic crust, we adopt a low constant viscosity of 10^{20} Pa s to decouple the slab from the top surface and the overriding plate (OP) and to facilitate subduction. A low viscosity of 10^{20} Pa s is also used in the weak layer as a weak mechanical coupling of the subducting and overriding plates with the lateral plate. The effects of varying this viscosity is shown in Figures 2e and S2. All model parameters are listed in table S1.

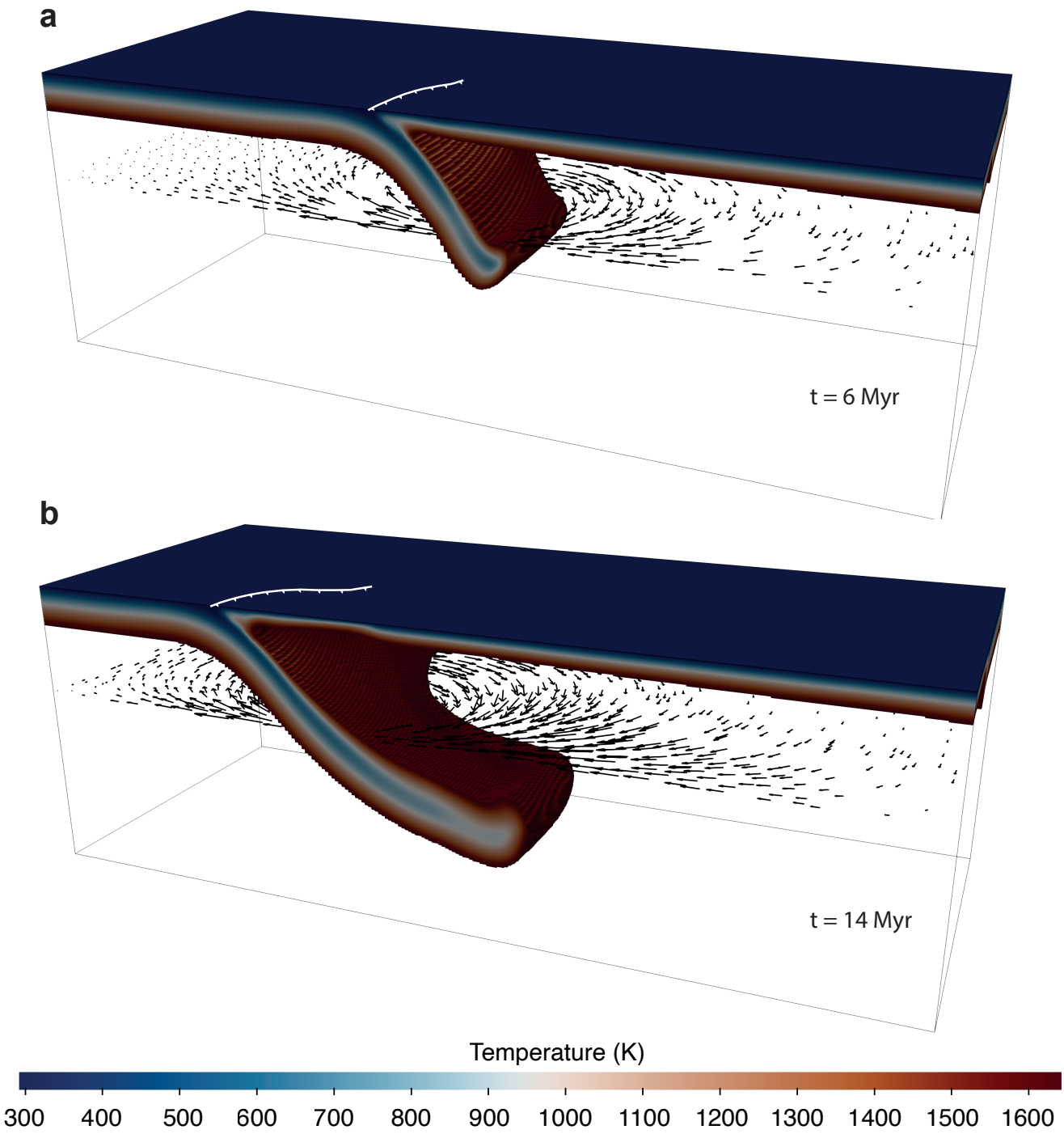

Figure S1. 3D perspective view of the subduction zone with the temperature field displayed for (a) 6 Myr and (b) 14 Myr. The figures are cutouts of the temperature between 293 K and 1500 K. White lines with triangles on the surface mark the trench position. Black arrows show the horizontal velocity field around the slab at 250 km depth.

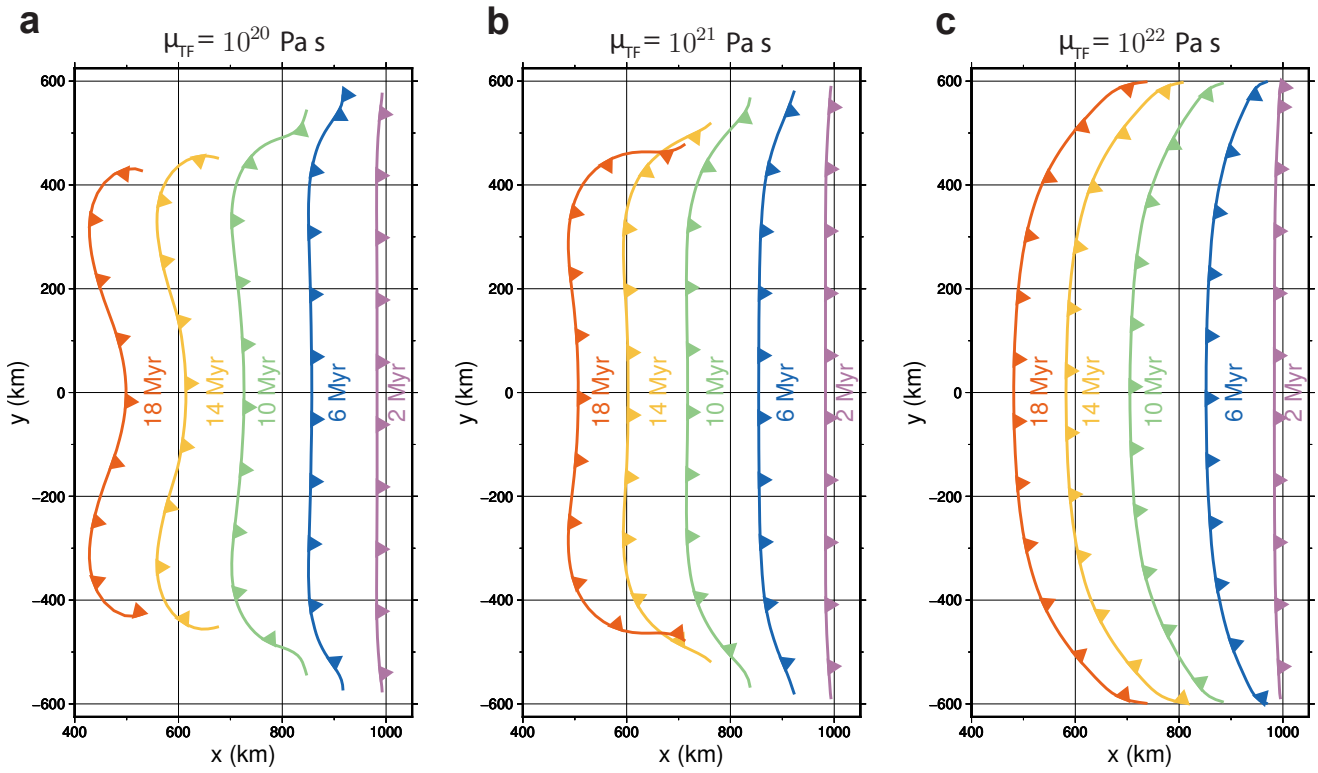

Figure S2. Evolution of the subduction trench for transform fault viscosities of (a) 10^{20} Pa s, (b) 10^{21} Pa s and (a) 10^{22} Pa s. The results shown correspond to models with overriding plate thicknesses of 70 km and slab widths of 1200 km (experiments 5, 10 and 15 in table S2).

Table S1. Model parameters

Symbol	Parameter name	Value	Units
Lithosphere and mantle rheology			
A	Exponential prefactor	$5.973 \cdot 10^{-16}$	$\mathrm{Pa^{-1}\,m^3\,s^{-1}}$
E	Activation energy	335	$\mathrm{kJ\,mol^{-1}}$
V	Activation volume	$4 \cdot 10^{-6}$	$\mathrm{m^3\,mol^{-1}}$
d	Grain size	10^{-2}	m
m	Grain size exponent	3	-
Overriding plate crust rheology			
A	Exponential prefactor	$5 \cdot 10^{-11}$	$\mathrm{Pa^{-1}\,m^3\,s^{-1}}$
E	Activation energy	170	$\mathrm{kJ\,mol^{-1}}$
V	Activation volume	0	-
d	Grain size	10^{-2}	m
m	Grain size exponent	3	-
Other model parameters			
ρ_{um}	Upper mantle density	3300	$\mathrm{kg\,m^{-3}}$
ρ_{lc}	Overriding plate crust density	2900	$\mathrm{kg\,m^{-3}}$
ρ_{oc}	Oceanic crust density	3300	$\mathrm{kg\,m^{-3}}$
ρ_{TF}	Transform fault density	3300	$\mathrm{kg\,m^{-3}}$
μ_{oc}	Oceanic crust viscosity	10^{20}	Pa s
μ_{TF}	Transform fault viscosity	10^{20}	Pa s
μ_{min}	Minimum viscosity	10^{19}	Pa s
μ_{max}	Maximum viscosity	$1.57 \cdot 10^{23}$	Pa s
c_p	Specific heat	1250	$\mathrm{J\,kg^{-1}\,K^{-1}}$
κ	Thermal diffusivity	$0.8 \cdot 10^{-6}$	$\mathrm{m^2\,s^{-1}}$
α	Thermal expansion coefficient	$3.5 \cdot 10^{-5}$	$\mathrm{K^{-1}}$
R	Gas constant	8.31	$\mathrm{J\,K^{-1}\,mol^{-1}}$
g	Gravitational acceleration	9.8	$\mathrm{m\,s^{-2}}$
T_0	Reference temperature	293	K

Table S2. Parameters examined in the numerical models

Experiment	**W/2 (km)**	**W (km)**	**OP thickness (km)**	$\boldsymbol{\mu_{TF}}(\mathbf{Pa \cdot s})$
1	200	400	70	10^{20}
2	300	600	70	10^{20}
3	400	800	70	10^{20}
4	500	1000	70	10^{20}
5	600	1200	70	10^{20}
6	200	400	70	10^{21}
7	300	600	70	10^{21}
8	400	800	70	10^{21}
9	500	1000	70	10^{21}
10	600	1200	70	10^{21}
11	200	400	70	10^{22}
12	300	600	70	10^{22}
13	400	800	70	10^{22}
14	500	1000	70	10^{22}
15	600	1200	70	10^{22}
16	300	600	40	10^{20}
17	300	600	50	10^{20}
18	300	600	60	10^{20}
19	300	600	80	10^{20}
20	300	600	90	10^{20}
21	300	600	100	10^{20}

Table S3. Data for narrow subduction zones used in Figures 4D and 4E. The subduction zone width (W) and trench retreat velocity (V_T) have been obtained from Schellart et al. (2007) (references therein). The overriding plate (OP) thickness has been obtained from different regional studies.

Subduction system	**W (km)**	**V_T (cm/yr)**	**OP thickness (km)**	**Reference OP thickness**
Gibraltar	250	0.9	100	Molina-Aguilera et al. (2019)*
Calabria	300	6.8	50	Rosenbaum and Lister (2004)
South Shetland	450	3.1	70	Parera-Portell et al. (2021)
Halmahera	500	7	50	Zhang et al. (2017)†
North Sulawesi	500	1.3	75	Dong et al. (2022)†§
Puysegur	750	4.2	59	Shuck et al. (2021)‡
Scotia	800	5.7	70	Fullea et al. (2021)¶
Sangihe	850	2.2	100	Fan and Zhao (2018)‖
Trobriand	900	7.6	55	Martinez et al. (2001)
Makran	900	0.2	90	Motaghi et al. (2020)
Manila	1000	5.7	80	Fullea et al. (2021)¶

*This value is obtained for the West Alboran Basin, near the trench.

†Based on numerical modelling.

§Models with OP 75 km thick best fit heat flux observations.

‡assuming that the crustal stretching factor β=1.7 obtained by Shuck et al. (2021) for the Solander basin stands for the entire lithosphere.

¶Temptatively from WinterC.

‖This value was also tested in the models of Zhang et al. (2017).

References From the Supporting Information

Bürgmann, R., & Dresen, G. (2008). Rheology of the lower crust and upper mantle: Evidence from rock mechanics, geodesy, and field observations. *Annual Review of Earth and Planetary Sciences*, *36*(1), 531-567. doi: 10.1146/annurev.earth.36.031207.124326

Dong, M., Lü, C., Zhang, J., & Hao, T. (2022). Downgoing plate-buoyancy driven retreat of north sulawesi trench: Transition of a passive margin into a subduction zone. *Geophysical Research Letters*, *49*(23), e2022GL101130. (e2022GL101130 2022GL101130) doi: 10.1029/2022GL101130

Fan, J., & Zhao, D. (2018). Evolution of the southern segment of the philippine trench: Constraints from seismic tomography. *Geochemistry, Geophysics, Geosystems*, *19*(11), 4612-4627. doi: 10.1029/2018GC007685

Fullea, J., Lebedev, S., Martinec, Z., & Celli, N. L. (2021, 03). WINTERC-G: mapping the upper mantle thermochemical heterogeneity from coupled geophysical–petrological inversion of seismic waveforms, heat flow, surface elevation and gravity satellite data. *Geophysical Journal International*, *226*(1), 146-191. doi: 10.1093/gji/ggab094

Hirth, G., & Kohlstedt, D. (2003, 01). Rheology of the upper mantle and the mantle wedge: A view from the experimentalists. *Washington DC American Geophysical Union Geophysical Monograph Series*, *138*, 83-105. doi: 10.1029/138GM06

Martinez, F., Goodliffe, A., & Taylor, B. (2001, 07). Metamorphic core complex formation by density inversion and lower-crust extrusion. *Nature*, *411*, 930-4. doi: 10.1038/35082042

Molina-Aguilera, A., de Lis Mancilla, F., Morales, J., Stich, D., Yuan, X., & Heit, B. (2019, 01). Connection between the Jurassic oceanic lithosphere of the Gulf of Cádiz and the Alboran

slab imaged by Sp receiver functions. *Geology*, *47*(3), 227-230. doi: 10.1130/G45654.1

Motaghi, K., Shabanian, E., & Nozad-Khalil, T. (2020). Deep structure of the western coast of the makran subduction zone, se iran. *Tectonophysics*, *776*, 228314. doi: 10.1016/j.tecto .2019.228314

Parera-Portell, J. A., de Lis Mancilla, F., Morales, J., Almendros, J., & Jiménez-Morales, V. (2021). Structure of the crust and upper mantle beneath the bransfield strait (antarctica) using p receiver functions. *Tectonophysics*, *802*, 228744. doi: 10.1016/j.tecto.2021.228744

Rosenbaum, G., & Lister, G. S. (2004). Neogene and quaternary rollback evolution of the tyrrhenian sea, the apennines, and the sicilian maghrebides. *Tectonics*, *23*(1). doi: 10.1029/ 2003TC001518

Shuck, B., Van Avendonk, H., Gulick, S. P. S., Gurnis, M., Sutherland, R., Stock, J., ... Hess, T. (2021). Strike-slip enables subduction initiation beneath a failed rift: New seismic constraints from puysegur margin, new zealand. *Tectonics*, *40*(5), e2020TC006436. (e2020TC006436 2020TC006436) doi: 10.1029/2020TC006436

Zhang, Q., Guo, F., Zhao, L., & Wu, Y. (2017). Geodynamics of divergent double subduction: 3-d numerical modeling of a cenozoic example in the molucca sea region, indonesia. *Journal of Geophysical Research: Solid Earth*, *122*(5), 3977-3998. doi: 10.1002/2017JB013991